

The Pacific Cold Tongue and the ENSO mode:
a unified theory within the Zebiak-Cane model

Paul C. F. van der Vaart and Henk A. Dijkstra
Institute for Marine and Atmospheric research Utrecht, The Netherlands

Fei Fei Jin
Department of Meteorology, University of Hawaii at Manoa

submitted to JAS September 19, 1998

Paul C. F. van der Vaart
Institute for Marine and Atmospheric research Utrecht
Department of Physics and Astronomy
Utrecht University, Princetonplein 5, 3584 CC Utrecht, The Netherlands
Phone: -31-30-2533276; Fax: -31-30-2543163
Internet: pvaart@fys.ruu.nl

Abstract

The equatorial Tropical Pacific Climate system is a delicate coupled system in which winds driven by gradients of sea surface temperature (SST) within the basin interact with the ocean circulation to maintain SST gradients. This results in a time-mean state having a strong zonal temperature contrast along the equator with an eastern cold tongue and a western warm pool. By the same coupled processes also interannual variability, known as El-Niño/Southern Oscillation, is present in the Pacific. This variability can be attributed to an oscillatory coupled mode, the ENSO mode, in the equatorial ocean/atmosphere system. Using a Zebiak-Cane type intermediate coupled model, the coexistence of an eastern cold tongue in the annual mean state and ENSO in the Pacific climate system are illustrated into one framework. The ENSO mode arises as a robust oscillatory mode on a coupled mean state and becomes unstable if the cold tongue of the mean state is sufficiently strong. The origin of this mode, its propagation mechanism, its sensitivity to parameters and its relation to the spatial structure of the annual mean state are considered.

1 Introduction

One of the first models by which the interannual variability in the Tropical Pacific, known as El Niño/Southern Oscillation, was reasonably simulated was that of Zebiak and Cane (1987). In this model, an annual mean state or seasonal cycle of both ocean and atmosphere is obtained from data and the evolution of anomalies with respect to this reference state are computed within the model. This coupled model produces recurring warm events that are irregular in both amplitude and spacing, but favor a 3-4 year period. Analysis of these results indicated that ENSO is a basin wide oscillation in the coupled ocean - atmosphere system. The Zebiak-Cane model and its variants (Battisti, 1988; Neelin, 1991) turn out to be very well suited to determine the details of the evolution of ENSO events and have been widely used to study the origin and physics of these events. Over the past decade, ENSO theory has advanced to a relative mature stage (Neelin *et al.*, 1997).

For a spatially constant annual mean state, Hirst (1986, 1988) found that oceanic equatorial modes can be destabilized by coupled processes. Further work into the nonlinear equilibration of these instabilities (Battisti and Hirst, 1989; Schopf and Suarez, 1988; Suarez and Schopf, 1988) lead to the BHSS delayed action oscillator paradigm (Schopf and Suarez, 1990). In this metaphor for ENSO dynamics, only one oscillatory mode is associated with the interannual variations on the annual mean state. The mode becomes unstable at sufficiently large coupling strength due to the Bjerknes feedback. It equilibrates due to nonlinear effects and ocean adjustment processes cause a delayed negative feedback, with central importance for a reflection of Rossby waves along the western boundary. These processes can be modeled within one nonlinear differential delay equation. Alternative simple models, e.g. the coupled wave oscillator model, were derived from point coupling models which combine the Bjerknes feedback with linear wave dynamics (Cane *et al.*, 1990; Münnich *et al.*, 1991).

In this view, the ENSO mode arises as an ocean dynamics mode which is destabilized by coupled processes and for which adjustment processes of sea surface temperature are unimportant (the fast SST limit). However, it appeared that interannual oscillations can also occur (Neelin, 1991) even when ocean wave time scales are very fast compared to those determining the SST field (the fast-wave limit). These SST (or thermal) modes (which decay when there is no ocean dynamics) are modified through ocean-atmosphere dynamics and can be destabilized through coupled processes. Hence, coupled ocean -atmosphere models may exhibit a variety of different oscillatory modes depending on the conditions set by parameters in the model.

In the uncoupled case, distinct sets of modes occur that are primarily related to the time scales of SST change (SST-modes) and that of time scales of ocean adjustment (ocean dynamics modes). The connection between both classes of modes in parameter space was explored by Jin and Neelin (1993a,b) and Neelin and Jin (1993) in a Zebiak-Cane type model using an equatorial strip approximation for the SST equation. At realistic coupling strength, the coupled

modes are best described by mixed SST/ocean-dynamics modes. The spatial structure of the ENSO mode is set by properties of a stationary SST mode which is unstable over a large range in parameter space at strong coupling. On the weaker coupling side, this mode merges with oscillatory modes originating from ocean-dynamics. In this way, ocean subsurface dynamics controls the period of oscillation. This standing-oscillatory regime as a standing SST mode perturbed by ocean wave dynamics provides a framework of understanding ENSO as an unstable coupled mode.

However, the picture of the mergers of the different modes is very complicated in the realistic regime (Jin and Neelin, 1993a). Reason for this is the presence of resolution dependent modes (called scatter modes) in the shallow water model on the equatorial β -plane arising from discretization of an essentially continuous spectrum (Moore, 1968). The classical ocean basin modes (Cane and Moore, 1981) arise as peaks in this spectrum. Hence, there is a desire to develop more simple models capturing the essentials of the ENSO mode. In a two-strip approximation of the shallow water dynamics, Jin (1997b) shows that all adjustment due to the scatter modes is described within one stationary mode. As coupling is increased this mode merges with a stationary SST mode to give an oscillatory unstable mode. The resulting mode has the property that the zonally averaged thermocline anomaly and the eastern Pacific SST anomaly are not in phase. At the transition phase of zero SST-anomaly, the average thermocline depth is shallower or deeper than its climatological value. Hence, within one cycle of the oscillation the equatorial heat content is discharged and recharged once. These features had been observed in data (Wyrtki, 1975) and in models (Cane, 1992), and have lead to a new view of the ENSO mode as a recharge oscillator. Jin (1997b) shows that both ocean wave oscillator, BHSS delayed oscillator and recharge oscillator can be derived from the two-strip approximation using reasonable assumptions. Furthermore, each basic oscillation can be captured by a simple two-dimensional dynamical system (Jin, 1997a). This unifies the different paradigms of the oscillatory nature of the ENSO mode and it is simultaneously consistent with the Jin and Neelin (1993a) picture of the unstable modes, although the spectrum of scatter modes has been considerably reduced.

In all studies cited above, the annual mean state is prescribed, for example by using flux-correction, and independent of coupled processes governing the ENSO mode. In reality, coupled processes also determine the annual mean state (and the seasonal cycle). A relatively small zonally constant windstress, which is thought to arise from factors outside the basin causes a weak zonal SST gradient, which is amplified by coupling to give the zonal equatorial warm pool/cold tongue structure. This was recently referred to as the "climatological version of the Bjerknes hypothesis" (Dijkstra and Neelin, 1995a). Again, an intermediate model was successfully used to demonstrate this and to identify areas in parameter space (coupling strength, atmospheric damping strength and surface layer feedback strength), where a fully coupled climatology can be found (Dijkstra and Neelin, 1995a) with the correct east-west structure. It was also shown that this state is unique and that previously found regimes of

multiple steady states are an artifact of the flux-correction procedure (Neelin and Dijkstra, 1995).

The stability properties of the fully coupled mean states may differ considerably from their flux-corrected counterparts. When coupling is varied, the basic state changes simultaneously with the most unstable perturbations. The absence of multiple equilibria, i.e. transcritical bifurcations, forbids the existence of a neutral stationary SST-mode which appears central in the Jin and Neelin (1993a) picture. Hence, one may question whether the ENSO mode is also strongly modified in the fully coupled case. This question was first addressed by Jin (1996) using the simple (box) recharge oscillator model. In this fully coupled model, oscillatory instabilities still persist and have ENSO characteristics. The stability of coupled annual mean states has been investigated in the Jin and Neelin (1993a) model by Dijkstra and Neelin (1998). In this case, the ocean dynamics spectrum is filtered such that only ocean basin modes remain. It turns out that a mixed SST-ocean dynamics mode is able to destabilize, but both its structure and period appear very sensitive to parameters. Apparently, one can no longer easily destabilize this mode, since in the regime where this is possible, the climatology has no correct zonal structure. This is in contrast with the results in flux-corrected models, where this regime can always be found, because the climatology is a solution for all values of the coupling strength.

In this paper, we study the stability of fully coupled climatologies within a model which closely approximates the Zebiak-Cane model. Simultaneous sensitivity of annual mean state and ENSO mode is determined by using techniques of numerical bifurcation theory (Dijkstra and Neelin, 1995b). The model is briefly described in section 2. In section 3, it is shown that ENSO-like unstable modes exist on a fully coupled climatology which has a reasonable warm pool/cold tongue structure. The stability of this climatology is investigated and modes are traced in parameter space to clarify their origin. In section 4, the robustness of these results is examined. A topological view of the ENSO mode is presented and compared to that in the flux-corrected models (section 5). In the last section the results are summarized.

2 The fully coupled Zebiak-Cane model

The formulation of the Zebiak-Cane model is well described elsewhere and in this section, only the differences with the standard set-up, the scaling and the final dimensionless equations which are solved are mentioned. The ocean model consists of a shallow water layer of mean depth H with an embedded mixed layer of fixed depth H_1 in an ocean basin which has zonal length L and is meridionally unbounded. The flow in the shallow water layer with velocity field (u, v, w) is determined by a reduced gravity model in the long wave limit and forced by windstress vector $\boldsymbol{\tau}$. Friction in the shallow water component is linear with damping coefficient r^* . The zonal velocity vanishes at the eastern boundary and a zero mass flux condition is applied at the western boundary; all quantities are bounded far from the equator. The mixed layer flow (with

velocity field (u_s, v_s) is determined from an Ekman layer model driven by the same windstress τ ; damping is also linear with damping coefficient ϵ_s^* .

The ocean model is coupled to a Gill (1980) atmosphere model with horizontal velocities (u_a, v_a) , geopotential height ϕ and with linear damping coefficient A^* . Windstresses are linearly related to surface velocities with coefficient γ_τ . The atmosphere is driven by heat fluxes from the ocean which depend linearly on the sea surface temperature T with proportionality constant α_T . Ocean processes determine the sea surface temperature and which is modeled by the SST-equation:

$$\partial_t T + \epsilon_w(T - T_0) + \frac{w_1}{H} \mathcal{H}(w_1)(T - T_{sub}(h)) + u_1 \partial_x T + v_1 \partial_y T = 0 \quad (1)$$

where $u_1 = u_s + u$ and $v_1 = v_s + v$ are the horizontal velocities in the mixed layer, $w_1 = w_s + w$ the vertical velocity just below the mixed layer and T_0 is the radiation equilibrium temperature. Newtonian cooling is represented by a coefficient ϵ_w and \mathcal{H} is the Heaviside function. The subsurface temperature $T_s(h)$ depends on h according to

$$T_s(h) = T_{so} + (T_0 - T_{so}) \tanh\left(\frac{h + h_0}{H_*}\right) \quad (2)$$

where h_0 and H_* control the steepness and the offset of the T_s profile and T_{so} is the characteristic temperature being upwelled into the surface layer.

The governing scales are nondimensionalized using scales for zonal length L , meridional length L_y , vertical length H , time L/c_0 , horizontal velocity c_0 , meridional velocity $c_0 L_y/L$, vertical velocity $c_0 H_1/L$, thermocline depth H_1 and temperature ΔT . Here, $c_0 = \sqrt{g'H}$ the phase speed of the first oceanic baroclinic Kelvin mode and L_y is the oceanic internal Rossby deformation radius. For the atmosphere, the meridional length scale is taken as L_a and both the zonal and meridional velocity are scaled with c_a . The final non-dimensional equations for the shallow water component become

$$(\delta \partial_t + r)u - yv + \partial_x h = \tau^x \quad (3a)$$

$$yu + \partial_y h = \tau^y \quad (3b)$$

$$(\delta \partial_t + r)h + \partial_x u + \partial_y v = 0 \quad (3c)$$

with the appropriate boundary conditions:

$$\int_{-\infty}^{\infty} u(0, y, t) dy = 0 \quad u(1, y, t) = 0 \quad (3d)$$

For the surface layer, the equations are

$$\epsilon_s u_s - y v_s = \gamma_s \tau^x \quad (4a)$$

$$\epsilon_s \Lambda_s^2 v_s + y u_s = \gamma_s \Lambda_s \tau^y \quad (4b)$$

The non-dimensional atmosphere model can be written as

$$\epsilon_a u_a - y_a v_a + \partial_x \phi = 0 \quad (5a)$$

$$y_a u_a + \partial_{y_a} \phi = 0 \quad (5b)$$

$$\epsilon_a \phi + \partial_x u_a + \partial_{y_a} v_a = -Q(x, y_a, t) \quad (5c)$$

and the dimensionless SST-equation is given by

$$(\delta_{sst} \partial_t + \epsilon_T) T - \epsilon_T T_0 + u_1 \partial_x T + v_1 \partial_y T + \alpha_w M(w_1)(T - T_{sub}(h)) = 0 \quad (6)$$

$$M(z) = \frac{1}{2} z (1 + \tanh(\frac{z}{\delta_w}))$$

$$T_{sub}(z) = T_{s0} + (T_0 - T_{s0}) \tanh(\eta_1 z + \eta_2)$$

As in Neelin and Dijkstra (1995), the dimensionless zonal wind stress forcing τ^x is decomposed into

$$\tau^x = \tau_{ext}^x + \mu u_a(x, y, t), \quad (7)$$

for the shallow water component (3), where the meridional windstress component τ^y is neglected. The windstress part indicated by τ_{ext}^x is considered to originate from factors outside of the basin and the quantity μ is the coupling strength. For the forcing of the surface layer (4), an extra parameter δ_s is introduced,

$$\tau^x = \tau_{ext}^x + \mu \delta_s u_a(x, y, t) \quad , \quad \tau^y = \tau_{ext}^y + \mu \delta_s v_a(x, y, t). \quad (8)$$

The parameter δ_s measures the effect of the Ekman velocities on the SST evolution through coupled feedbacks, as in Jin and Neelin (1993a). The forcing Q for the atmosphere is proportional to the SST deviation from the radiation equilibrium temperature T_0 , i.e. in dimensionless quantities

$$Q = T - T_0 \quad (9)$$

The expressions for dimensionless parameters in the equations in terms of dimensional parameters and their standard values are given in Table 1. In comparison to the original parameter values in Zebiak and Cane (1987), the most important differences lie in the T_{sub} parameterization and the reference phase speeds of both the oceanic c_o and atmospheric c_a Kelvin wave, with $c_o = 2 \text{ m/s}$ and $c_a = 30 \text{ m/s}$ versus $c_o = 2.9 \text{ m/s}$ and $c_a = 60 \text{ m/s}$.

The numerical details for solving the set of equations (3)- (6) can be found in Appendix A. Variables are expanded into spectral basis functions, with Chebychev polynomials in zonal direction and Hermite functions in meridional direction. Using collocation techniques a set of nonlinear algebraic equations is obtained for the steady states of the model. The analysis of the stability of these steady states leads to a generalized eigenvalue problem. Both steady states and their linear stability are traced through parameter space using continuation techniques as described in Dijkstra and Neelin (1995b).

3 The warm pool/cold tongue and its bifurcation to ENSO

3.1 The fully coupled steady state

At zero coupling ($\mu = 0$), the ocean circulation and consequently SST is determined by the external zonal windstress τ_{ext}^x . This windstress is assumed to have the form

$$\tau_{ext}^x = -F_0 e^{-\frac{(\alpha y)^2}{2}} \quad , \quad \tau_{ext}^y = 0 \quad (10)$$

where α is the ratio of Rossby deformation radii between ocean and atmosphere which controls the meridional extension of the external wind. The amplitude F_0 has a standard value of 0.2, corresponding to a dimensional value of 0.01 Pa. At each latitude, the external wind is zonally constant. As discussed in detail in Dijkstra and Neelin (1995a), this easterly windstress is interpreted as that part of the windstress which does not depend on the coupled feedbacks within the basin. Even in the absence of longitudinal SST gradients, there would still be a Hadley and a Walker circulation, driven by zonally symmetric latitudinal gradients and zonally asymmetric land-sea contrast, respectively.

The resulting temperature field at zero coupling, T_{ext} , and thermocline depth h_{ext} are shown in Fig. 1. In response to the easterlies, the temperature decreases monotonically from about 25.5 °C in the east to about 28.5 °C in the west along the equator. The equatorial thermocline response is approximately linear, with slight off-equatorial maxima near the western boundary.

As the coupling μ is increased, coupled feedbacks induce an enhancement of the Pacific cold tongue structure. At low coupling, the additional windstress due to coupling is approximately the atmosphere response to the original cooling $T_{ext} - T_0$, which enhances the external easterlies over most of the basin, leading to larger upwelling and a stronger thermocline slope (Dijkstra and Neelin, 1995a) which gives a cold tongue in the eastern-central part of the basin. The temperature $(T - T_0)_{EC}$ of the cold tongue and the vertical velocity, w_E , just below the mixed layer both at $(x = 0.8, y = 0)$ (shown in Fig. 2) demonstrate that there is a unique steady solution as a function of μ , with a colder eastern Pacific and more upwelling as coupling gets stronger.

At $\mu = 0.5$, the spatial structure of the coupled climatology is shown in Fig. 3. The zonal scale of the cold tongue (panel a) is set by a delicate balance of thermocline and surface layer feedbacks (Dijkstra and Neelin, 1995a). The meridional extent of the cold tongue is determined both by the Ekman spreading length (ϵ_s^*/β) and by meridional advection. The thermocline field (panel b) is in Sverdrup balance with the windstress giving the off-equatorial maxima and a deeper (shallower) equatorial thermocline in the west (east). This indicates that the reservoir of heat content lies off-equatorial in the central and western part of the basin. The windstress response u_a (panel c) shows the intensification of the easterlies, with its maximum west of the cold tongue. This zonal spatial phase

difference is controlled by ϵ_a , its larger meridional scale is due to the atmospheric internal Rossby deformation radius, controlled by the parameter α . The vertical velocity structure (panel d) is clearly controlled by Ekman pumping which gives the positive values restricted to an equatorial zone with maximum amplitude in the eastern part of the basin.

3.2 Linear stability of the coupled climatology

As shown in Neelin and Jin (1993), the spectrum of the uncoupled system consists of SST modes and those related to the shallow water dynamics on an equatorial β -plane. The latter can be divided into ocean-basin modes and scatter modes which arise through discretization of the essentially continuous spectrum caused by the infinite extent of the domain in the meridional direction. The latter modes decay faster than the oceanic damping rate because energy leaks from the equatorial basin to higher latitudes.

Along a branch of steady states in Fig. 2 the linear stability is determined simultaneously, by writing the solution vector \mathbf{z} (cf. Appendix A) as

$$\mathbf{z}(x, y, t) = \bar{\mathbf{z}}(x, y) + \tilde{\mathbf{z}}(x, y) e^{\sigma t}. \quad (11)$$

The vector $\bar{\mathbf{z}}$ represents the climatology, $\tilde{\mathbf{z}}$ perturbations with respect to this climatology and σ is the corresponding eigenvalue. The numerical methods are similar to that of Dijkstra and Neelin (1995b) although different solvers were used in the generalized eigenvalue problem. In Fig. 4, the path of six modes, which become leading eigenmodes at high coupling is plotted as a function of the coupling strength μ in the complex plane. In panel (a), the modes are plotted in the same way as in Jin and Neelin (1993b), with a larger dot size indicating a larger value of μ . Both period and growth rate of the modes are given in year^{-1} . In panel (b) only the growth rate is plotted against μ .

There is one stationary mode which is the gravest mode at $\mu = 0$ but its decay rate is nearly constant in μ . An oscillatory mode becomes unstable near $\mu = 0.503$. This mode can be traced back to $\mu = 0$ and appears to deform into one of the scatter modes of the shallow water model. Other modes appear hardly affected by coupling. The gravest ocean-basin mode (marked with triangles) is heavily damped as μ is increased (Fig. 4(b)). The SST-modes remain damped and none of these modes was found to be interacting with the ocean dynamics modes as in the flux-corrected case (Jin and Neelin, 1993a). The SST-modes reside in the spectrum to the left of the modes shown in Fig. 4(a). More details on the complete spectrum can be found in Appendix B.

Near $\mu = 0.503$, for which the mean state was shown in Fig. 3, time-longitude diagrams of the equatorial thermocline, temperature and zonal wind anomalies of the most unstable mode are shown in Fig. 5. Note that the amplitude of the oscillation is not determined by a linear stability analysis. The maximum amplitudes in the captions are relative magnitudes of the different fields, i.e. the mode displays a thermocline deviation of about 10 m per degree SST anomaly.

The SST pattern displays a nearly standing oscillation for which the spatial scale is confined to the cold tongue position of the mean state. There is slight

eastward propagation of the SST anomaly in the central equatorial Pacific. The thermocline anomaly shows western anomalies in heat content leading the eastern ones with the separation between positive and negative anomalies occurring within the front defined by the cold tongue; it is out of phase with the SST anomaly with a lag of about 5 months. The wind response is much broader zonally and is in phase with the SST anomaly. Although the wind maximum in the central Pacific is more to the east with respect to observations, all fields do correspond reasonably to those observed (Latif *et al.*, 1993; Neelin *et al.*, 1994).

The phase relationships between wind/SST-anomalies and thermocline anomalies are investigated in more detail through Fig. 6 where the thermocline depth in the western Pacific h_W as well as the zonal mean equatorial thermocline displacement h_{ZM} is related to the SST anomaly in the eastern Pacific (at $x = 0.92$) over one cycle of the oscillation. At this particular location, the temperature anomaly (Fig. 5) has largest amplitude. Panel (a) shows the characteristic ENSO phase relationship between SST and thermocline anomalies with a relatively shallow (deep) thermocline in the west in case of a warm (cold) event.

As the closed curve is traversed clockwise over one cycle of the oscillation, one clearly observes that a cold event is followed by an extremum in western thermocline anomaly. As the SST anomaly becomes zero, the western thermocline anomaly is positive in the west and panel (b) shows that this also holds for the zonally averaged thermocline anomaly. Hence, the equatorial heat content is slowly built up after the cold event by the increase of the trade winds. This sets the stage for the following warm event in which the equatorial heat content is discharged. After the warm event, the zonally averaged thermocline anomaly is negative as the SST anomaly goes through zero again and the equatorial heat content is low, which causes the next cold event.

Clearly, the phase relationships between the different fields of the ENSO mode are in qualitative agreement with the recharge oscillator as described in Jin (1997a). Central to this picture are the non-zero zonally averaged thermocline anomalies which occur simultaneously with zero eastern SST anomalies and therefore out of phase with the windstress anomalies. When the trades are relaxed during each transition phase between warm and cold events, anomalous cold or warm water can be pumped into the surface layer, to establish the transition from cold to warm anomalous SST. Exactly these phase relationships seem to be involved in ENSO modes in the Zebiak-Cane model (Zebiak and Cane, 1987; Kirtman, 1997).

3.3 Recharge oscillation mechanism of the ENSO mode

In a way, the results presented here are the first of its kind to capture a well-resolved meridional extent of the eigenmode of the coupled system. This meridional structure of the ENSO mode appears important for its period and therefore the propagation mechanism of the oscillation is described in detail. This is done along with plots of the different fields at several phases of the oscillation relative to the period, i.e. phase $t = 1/2$ indicates the fields after half a period. In the Figs. 7 to 9, these plots are given for the temperature, thermocline and zonal

wind field, respectively.

The starting point of the description of the self-sustained oscillation is a positive SST-anomaly (SSTA) in the eastern Pacific (early El-Niño phase), as shown in Fig. 7 at $t = 0$. Westerly zonal wind anomalies to the west of the maximum in SSTA (Fig. 7) are present as can be seen in Fig. 9 at $t = 0$. The wind response amplifies the positive SSTA through the Bjerknes' feedback ($t = 1/16$ to $1/8$). The extent of the SST anomaly is controlled by the climatological shape of the cold tongue in both the zonal and meridional direction (cf. Fig. 3).

The equatorial thermocline response to the weaker tradewinds up to $t = 1/8$ results in a negative anomaly (i.e. negative heat content) in the Western Pacific (Fig. 8, $t = 1/8$), which is at its minimum a few months later than the maximum of equatorial SST. As long as the positive thermocline/SST-anomaly in the eastern part of the basin does not weaken, this negative anomaly cannot be discharged. However, due to ocean wave reflections at the eastern boundary, the mass fed along the equator to the eastern basin is transformed into a collective of long Rossby waves. The position of the off-equatorial maximum in the thermocline anomaly is predominantly controlled by the ratio of Rossby deformation radii between ocean and atmosphere as will be shown below.

At the equator, the positive thermocline anomaly and consequently the SST anomalies are weakened. This reduces the east-west SST gradient, causing the anomalous westerlies to slacken (Fig. 9, $t = 1/8$ to $5/16$). Termination of the El Niño phase sets in, as the western warm pool discharges its previously built up negative heat content ($t = 3/8$ through $7/16$ in Fig. 8). This is characteristic of the recharge oscillator, showing a negative zonally mean thermocline anomaly at the equator during the transition from warm to cold SST anomalies. As the thermocline rises in the east, the SST anomaly becomes negative and through Bjerknes' feedbacks its amplitude increases. The trade winds recover (Fig. 9, $t = 7/16$) and the positive off-equatorial thermocline anomalies propagate westwards (Fig. 8, $t = 3/8 - 7/16$).

The evolution of the meridional structure of the anomalies in the eastern Pacific (at $x = 0.85$) indicates (Fig. 10) that the largest SST anomalies are confined to the equator and the off-equatorial anomalies are in phase and have the same sign as those at the equator, but are substantially weaker. The wind anomalies have a much broader structure and off-equatorial wind anomalies are out of phase with the equatorial ones. The thermocline anomalies display a nice parabolic shape (as for instance assumed in the 2-strip model of Jin (1997a)). The apparent away-equator propagation is due to the fact that Rossby wave propagation speed decreases with latitude.

Time longitude diagrams of the thermocline anomalies and meridional geostrophic velocities at 8 N ($y = 3.8$) and the anomalous windstress curl at that particular latitude are shown in Fig. 11. The reflected Rossby wave originating at the eastern boundary are overtaken by the forced Rossby waves (Fig. 11a). Both reflected and forced Rossby waves contribute to the recharge and discharge of the equatorial thermocline. When the windstress reaches zero from a positive (negative) anomaly (Fig. 11c), the Rossby waves continue to propagate and thus

the equatorial heat content continues to discharge (recharge) (Fig. 11b). It is this interval in the ocean dynamical adjustment to a changing windstress, that is responsible for the ENSO phase transition.

4 Robustness

Of central importance to the results above is the simultaneous existence of a sufficiently strong east-west temperature contrast, i.e. a correct warm pool/cold tongue structure and a realistic ENSO mode. In the filtered model of Dijkstra and Neelin (1998) where only ocean basin modes were allowed in the ocean dynamics spectrum, this simultaneous existence turned out to be very sensitive to parameters. For example, if the coupling strength was slightly increased from a correct situation, either the character of the ENSO mode or the climatology very soon became unrealistic.

It will be shown below that in the fully coupled model used here, sensitivity is small. Both the correct climatology and the spatial structure of the ENSO mode at criticality, i.e. at the primary Hopf bifurcation, appear to be a very robust feature. In the next subsections, the model parameters ϵ_a , δ_s , α and F_0 will be changed one at a time. The path of the Hopf bifurcation will be followed simultaneously with the climatology, which can be efficiently performed by continuation methods.

4.1 The meridional extent of the wind response

The path of the Hopf-bifurcation point in the (α, μ) plane and the period of oscillation at criticality are shown in Fig. 12(a) and (b). A larger value of α indicates a smaller atmospheric meridional response and for $\alpha \rightarrow 1.0$, the atmospheric meridional scale more and more resembles that of the ocean. With increasing α , the spatial structure of the climatology changes to become more stable, i.e. one needs a larger coupling strength to excite the ENSO mode. The ENSO-period decreases from about 4 years at $\alpha = 0.2$ to 2 years at $\alpha = 0.7$. This result is in agreement with recent results of Kirtman (1997), who found that a broader meridional wind response leads to longer ENSO periods. For $\alpha = 0.7$, the SST climatology at the Hopf bifurcation $\mu = 2.5$ (shown in Fig. 13a) shows that the spatial structure of SST is much more confined to the equator. Compared to the case $\alpha = 0.2$, the wind response is weaker and the thermocline in the east is deeper, leading to a warmer cold.

The same equatorial confinement is seen in the SST structure of the ENSO mode at the equator (panel (b)) and the discharge of equatorial heat content is more gradual (panel (c)). The spatial pattern of temperature, thermocline and zonal wind anomaly are shown in panel (d), (e) and (f) of Fig. 13, at phase $t = 0$ of the oscillation. A more localized wind response prevents that the higher order Rossby modes get excited. The consequence is that only low order Rossby modes provide the westward propagating signal in the ocean in this case predominantly the $n = 1$ mode. The resulting period is the two years shown in

Fig. 12. At smaller α , higher order modes contribute to the propagation of the thermocline anomalies westward and the period of the oscillation is increased. In the entire regime, the oscillation mechanism is the same as the recharge oscillator discussed in section 3.3. The sensitivity of the period to α can be understood in terms of the ocean adjustment time scales to different meridional structures of the windstress. This time scale is relatively shorter for a larger α than that for small α . In fact, the dependence of the period and stability on α as shown in Fig. 12 can be understood qualitatively using the conceptual model of Jin (1997a) by examining the dependence of the ocean adjustment time scale of the model on α .

4.2 The strength of the external windstress

The path of the Hopf bifurcation in the (μ, F_0) plane in Fig. 14(a) indicates that the period and stability do not depend much on the value of F_0 if its value is larger than 0.2. For small F_0 , there is not sufficient upwelling to generate a correct cold tongue (Dijkstra and Neelin, 1995a), making the climatology more stable. This incorrect spatial structure of the climatology has also severe consequences for the spatial pattern of the most unstable mode, although the period of the oscillation (panel (b)) is not affected much down to $F_0 = 0.1$.

Too large values of F_0 make the eastern basin too cold because of coupled feedbacks on the zonal SST gradient the latter created by the external windstress. The amplitude of the cold tongue for $F_0 = 0.4$ has increased to about 11 degrees (Fig. 15a), it is confined more to the eastern boundary and has a broader meridional extent. This is immediately reflected in the structure of the SST anomaly of the ENSO mode (Fig. 15b,d). However, there is little impact on the (Fig. 15c,e)thermocline anomalies and hence on the period of the oscillation.

The amplitude and shape of τ_{ext} are hard to determine from observations. Although GCM runs to get an impression of these quantities have been proposed (Dijkstra and Neelin, 1995a), there is no justification for their assumed shape and amplitude. Fortunately, the period of the ENSO mode is only weakly dependent on the particular details of τ_{ext} . One needs a sufficient externally induced SST gradient to get a correct cold tongue and hence F_0 should not be too small. Once this has been established, the spatial pattern of the ENSO mode depends on the pattern of the cold tongue, but its period is hardly affected.

4.3 Surface layer processes

There is only a weak dependence of the location of the Hopf bifurcation (Fig. 16) on the parameter δ_s , within the range 0.2 – 0.6, controlling the influence of coupled processes within the surface layer response. The period slightly decreases with δ_s and the stability boundary in μ of the climatology slightly decreases simultaneously.

For small values of this parameter, the cold tongue is strongly confined to the eastern boundary (Dijkstra and Neelin, 1995a). Hence, the subsurface

thermocline is already near saturation and a large coupling is needed to induce instability. As δ_s is increased, the eastern part of the basin tends to warm due to the upwelling feedback (less upwelling near the eastern boundary) which can be clearly seen in Fig. 17a for $\delta_s = 0.6$. The maximum easterly wind response has shifted slightly westward, leading also to a slightly deeper thermocline in the east. These feedback processes make the climatology very unrealistic for large δ_s . Although again the SST anomalies are confined to the cold tongue (Fig. 17b,d), the spatial pattern of the thermocline anomalies hardly differs from the standard case (panel (c, e)). The windstress anomalies (Fig. 17f) appear slightly more confined to the equator, which leads to higher wave mode contributions in the off-equatorial response and consequently a smaller period.

4.4 Atmospheric damping length

When ϵ_a is increased from 0.5, the period of oscillation is not sensitive but the climatology stabilizes (Fig. 18). The reason for the stabilization with increasing ϵ_a is again the confinement of the equatorial tongue to the east (Fig. 19a) leaving a smaller area where coupling can be effective. The mechanisms of the displacement of the cold tongue with ϵ_a were discussed in Dijkstra and Neelin (1995a). Basically, the wind response becomes more localized to the SST field, with maximum easterly wind closer to maximum SST anomalies, leading to a shift of negative thermocline anomalies eastward.

Sea surface temperature anomalies of the ENSO mode are therefore confined to the eastern boundary for large ϵ_a , as can be seen in figure 19(b,d), the wind response of the mode is more localized (panel (f)), but the structure of the thermocline anomalies (panels c and e) is not affected much and hence the period is not very sensitive to ϵ_a .

5 Topological view on the coupled mode

The results in the previous section indicate that the stability of the climatology with respect to the ENSO mode is controlled by the shape of the cold tongue. On the other hand, the period of the mode seems to be determined by ocean adjustment timescales which depend on the contribution of the higher order Rossby modes to the transport of information westwards. Physically, the ENSO mode can be understood as a recharge oscillator. Topologically, the mode appears to connect to one of the ocean dynamics scatter modes in the small coupling limit, as shown in section 3.2.

From the Jin and Neelin (1993a) framework to understand the origin of the ENSO modes, albeit in the flux-corrected case and using an equatorial strip approximation for the SST, a stationary SST-mode is the dominant unstable mode at large coupling. This stationary mode was argued to be connected to an SST mode in the fast wave limit (i.e. $\delta \rightarrow 0$ in their Fig. 22). Hence, by connection of the eigensurfaces of both type of modes, the resulting ENSO-mode was characterized as a mixed SST/ocean-dynamics mode.

The appearance of the unstable stationary mode was shown to be related to a transcritical bifurcation in Hao *et al.* (1993) and Dijkstra and Neelin (1995b). However, these transcritical bifurcations are not robust when coupling influences the mean state. The multiple steady state structure in the flux-corrected models thereby disappears (Dijkstra and Neelin, 1995a). Consequently, the stationary SST mode cannot become neutral in the fully coupled case. The question therefore remains whether the ENSO mode in the fully coupled case can again be characterized as a mixed SST/ocean-dynamics mode.

To get as close as possible to the Jin and Neelin (1993a) results, their parameters in the T_{sub} parameterization have been chosen. In comparison to the standard case as in Table 1, both qualitative and quantitative changes in structure and period of the climatology and ENSO-mode are small. In Fig. 20, the path of the leading eigenvalues as a function of coupling is shown for the fully coupled case. The basic structure of the modes corresponds well to that in the standard case, with one mode arising out of a bundle of ocean dynamics modes as coupling is increased and becoming unstable at about $\mu_H = 0.4$. At high coupling ($\mu = 0.7$) the oscillatory ENSO-mode breaks up into two stationary modes. For both modes, one with an increasing and one with a decreasing growthrate, the growthrate remains positive as it should be. For the mode to stabilize at larger μ , it would have to become oscillatory first.

The effect of flux-correction is investigated by taking the reverse path than the one taken in Neelin and Dijkstra (1995), which went from flux-corrected to fully coupled climatology. The climatology as in Fig. 3 obtained at $\mu = \mu_H$, indicated by \bar{T} for the SST field, is taken as a reference state to which flux-correction is applied. The prescribed windstress generating this climatology, say τ_{obs}^x , is obtained from the fully coupled model as

$$\tau_{obs}^x = \tau_{ext}^x + \mu_H A(\bar{T} - T_0) \quad (12)$$

Next, the atmosphere model operator is changed such that it is only forced by SST anomalies with respect to this reference state. The path between both model formulations is then defined by a homotopy parameter α_h and given by

$$\tau^x = (1 - \alpha_h) [\tau_{obs}^x + \mu A(T - \bar{T})] + \alpha_h [\tau_{ext}^x + \mu A(T - T_0)] \quad (13)$$

In the flux-corrected case ($\alpha_h = 1$), the paths of the leading eigenvalues with μ are shown in Fig. 21. In this case, the location of the primary Hopf bifurcation is (by construction) identical to that in the fully coupled case ($\alpha_h = 0$). At higher coupling, the same bifurcation to stationary modes appears, but the growthrate of the lower stationary mode becomes negative. This corresponds to a transcritical bifurcation as a secondary bifurcation of the flux-corrected climatology which leads generically to multiple equilibria. This is comparable to the earlier results found in Neelin and Dijkstra (1995) in a simpler model, demonstrating the occurrence of artificial stationary bifurcations due to flux-correction in this more complete version of the Zebiak-Cane model. For this

particular parameter regime the multiple equilibria are expected to be unstable, and consequently the actual impact of the transcritical bifurcation on the limit-cycle arising from the Hopf bifurcation may be small.

The oscillatory mode seems to have the same nature in the flux-corrected and fully coupled cases. The relation of the modes with those in the fast wave limit ($\delta = 0$) is shown in Fig. 22 and Fig. 23 for both flux-corrected and fully coupled cases respectively. In both cases, the coupling strength has been increased to $\mu = 0.75$, and the oscillatory mode has already bifurcated into two stationary modes. Note that for both cases, the climatologies are different then, because for the fully coupled case this state depends on coupling, whereas for the flux-corrected case it is fixed.

As δ is decreased from its standard value $\delta = 1$ to the fast-wave limit $\delta = 0$, first the two real eigenvalues connect again and merge into an oscillatory mode near $\delta = 0.7$. As this mode stabilizes with decreasing δ , its frequency increases. At $\delta = 0.3$, the oscillatory mode becomes neutral and then rapidly decays with decreasing δ . In the fast-wave limit the modes remaining in the spectrum are all related to the SST-equation. However, there is no merger between the SST modes and the former oscillatory coupled mode as δ decreases to zero.

This view of the connection between fast-wave limit and regimes dominated by ocean basin adjustment processes does not depend on the use of flux-correction. The parameter δ does not affect the climatology. The differences between Fig. 22 and Fig. 23 arise from the different climatologies. In both cases an exchange of modes occurs near $\delta = 0.2$, but what might at first sight be interpreted from the growthrates (Fig. 23a) as a merger of the coupled mode and SST-modes, is clearly discarded as a merger when viewing the frequencies (Fig. 23b). More support for this result is found by plotting the dominant modes as a function of δ_{sst} (Fig. 24). The mode continues without merging to the fast-SST limit ($\delta_{sst} = 0$) and its period is hardly affected, except near $\delta_{sst} = 0$.

Our results strengthen the idea (Jin and Neelin, 1993a) that one mode, originating from an uncoupled ocean dynamics scatter mode, which gets destabilized through coupled processes, dominates the dynamics. Its timescale is set by ocean adjustment processes, and its spatial scale is heavily controlled by the climatology, instead of by the influence of SST modes. However, mixed layer processes contribute indirectly to the spatial structure of the ENSO mode, because no realistic climatology could have been obtained without them.

Within this view of the origin of the mode, the results of Jin (1997b) and of Dijkstra and Neelin (1998) can be considered as particular limits. In the 2-strip flux-corrected model of Jin (1997b), the ocean dynamics spectrum consists of ocean basin modes and one stationary adjustment mode representing the scattering spectrum in a heavily meridionally truncated model. To get a recharge oscillator, a merger between this adjustment mode and a stationary SST mode is necessary to guarantee the right phase relationships between zonally averaged thermocline anomalies and windstress anomalies. The former still plays an important role to give the mode its oscillatory features and the period of oscillation is therefore dependent on δ . In the analysis of Dijkstra and Neelin (1998), us-

ing a model in which the scattered modes are filtered, the final unstable mode arises through a connection of an oscillatory SST mode and an ocean dynamics mode, related to the gravest ocean basin mode at small coupling. However, it appeared that all characteristics of this mode are very sensitive to parameters and this mode is not likely to be robust, although the parameters can be tuned such that a correct climatology and a reasonable pattern of the ENSO mode appear.

No mergers between SST modes and ocean-dynamics modes were found here and moreover, the coupled mode arising from the gravest ocean basin mode does not seem to be important to induce an ENSO mode since it is heavily damped at large coupling. A rather simple picture of the origin of the ENSO-mode emerges if sufficiently spatial (meridional) resolution is provided to be able to represent the correct coupled mode and the climatology. When the unstable coupled mode is traced from large to zero coupling (Fig. 4) it connects to an ocean dynamics scatter mode. The sensitivity of this coupled mode to other parameters is small once the mean state and its instabilities are determined by the same processes.

6 Summary and Discussion

Tropical coupled general circulation models have reached the stage in which the ENSO cycle is realistically simulated within the multitude of other time-scale phenomena which occur in the model (Philander *et al.*, 1992; Terray *et al.*, 1995). Most models are also able to simulate a mean state which has correct amplitude and spatial structure. In these detailed models, both the ENSO cycle and mean state are determined by the coupled processes in the Pacific basin. An understanding of the result in terms of basic physical processes is necessary to determine a priori changes of this variability under different conditions.

Analysis of the effects of coupled processes in intermediate complexity models, such as the Zebiak-Cane model, have provided a framework to understand the origin of oscillatory coupled modes. When the mean state is prescribed, by some procedure referred to in general as flux-correction, the structure of the mixed SST/ocean dynamics modes provides this framework (Jin and Neelin, 1993a). When the cold tongue/warm pool structure is itself determined by coupled processes, the ENSO variability is connected to one robust coupled mode in the ocean-atmosphere system. The period of this mode is for quite a large volume in parameter space about four years, when the climatology has the correct spatial structure. Both the cold tongue steady state and the characteristics of the associated ENSO mode are very robust to variations of model parameters.

The spatial pattern of the climatology is important to set the location where amplification of disturbances can occur. Only SST-anomalies in the cold tongue can be amplified due to Bjerknes' feedback. As the cold tongue warms, the tradewinds relax, the equatorial thermocline tilt reduces, and the deepening of the east Pacific thermocline further amplifies the SST warming within the cold tongue. At the same time, as explained in more detail in section 3.3, the position

of the off-equatorial waves is just outside the cold tongue. In this way, mass is exchanged from the equatorial region towards off-equatorial latitudes. This causes the discharge of equatorial heat content which weakens the SST anomaly and thereby the wind anomaly. When the SST and wind anomalies diminish, this discharge process of equatorial ocean heat content continues, leading to an anomalously shallow thermocline over the entire equator. Upwelling is able to induce negative SST anomalies and therefore induces a cold phase of ENSO. This recharge oscillation mechanism, first envisioned by Wyrтки (1985) and Cane and Zebiak (1985), and later illustrated by Jin (1996, 1997a), is clearly consistent with the ENSO mode of the fully coupled model.

The ENSO mode we find has also features of the coupled wave oscillator model of Cane *et al.* (1990), since the coupled mode exists in the fast SST limit. On the other hand, it is not the gravest ocean basin mode which gets unstable at large enough coupling, but a mode which arises from the scatter spectrum of the shallow water model. Because of this, the coupled mode obtains the phase relations as in the recharge oscillator model as described by Jin (1997a). The simplification in spatial structure of Jin (1996, 1997a,b) requires the merger between a stationary ocean dynamics mode and an SST mode to form an oscillating mode as the recharge oscillator for ENSO. When detailed spatial structure is taken into account, it is the spatial structure set by the SST processes combined with the oscillatory oceanic scatter mode to form the recharge oscillation for ENSO. Therefore the picture portrayed in Jin and Neelin (1993a) and Jin (1996, 1997a) is reconciled.

This puts a firm basis under the thesis that oscillatory coupled modes dominate the dynamics in realistic models. When conditions are supercritical, a limit cycle (the ENSO oscillation) will be the dominant mode of internal variability. But even when this oscillatory mode is not unstable, i.e. μ is below the critical value for instability, it may be excited by stochastic forcing from the atmosphere (Blanke *et al.*, 1997). The degree of sub- or supercriticality is essential whether irregularity of the ENSO cycle can be attributed to deterministic processes, i.e. interaction with the seasonal cycle (Jin *et al.*, 1994; Tziperman *et al.*, 1994), or whether it is stochastically determined.

Acknowledgments

This work was supported by the Dutch National Research Programme on Global Air Pollution and Climate Change (N.R.P.) within project 951235. All computations were performed on the CRAY C916 at the Academic Computing Centre (SARA), Amsterdam, the Netherlands within project SC283. Use of these computing facilities was sponsored by the National Computing Facilities Foundation (N.C.F.) with financial support from the Netherlands Organization for Scientific Research (N.W.O). Collaboration was initiated during a visit of HD to UCLA (Los Angeles) and UH (Honolulu) in 1997 which was sponsored by NSF grant ATM-9521389 (J.D. Neelin) and a N.W.O. PIONIER grant (HD). FFJ is supported by NSF grant ATM-9312888. Discussions with David Neelin (UCLA) are much appreciated.

Appendix A: Numerical methods

To solve the equations (3) - (6) on the computational domain $(x, y) \in [0, 1] \times (-\infty, \infty)$, a pseudo-spectral approach is followed. The dependent quantity $T - T_0$ is thereto expanded as

$$T(x, y, t) - T_0(x, y, t) = \sum_{i=0, j=0} f_{ij}(x, y) q_{ij}(t) \quad (A.1)$$

where the basisfunctions f_{ij} are given by

$$f_{ij}(x, y) = C_i(2x - 1)\psi_j(y) \quad (A.2)$$

where y is the oceanic meridional coordinate, the ψ_j are the Hermite functions and the C_i are the Chebychev polynomials defined by

$$C_i(x) = \cos(\text{iarccos}(x)) \quad , \quad i = 0, \dots, N_x.$$

The atmospheric response to an arbitrary heat flux forcing Q is determined by writing $u_a = R + S$ and $\phi = R - S$ in (5). The variables R , S and V and the forcing term $Q = T - T_0$ are expanded into Hermite functions with the atmospheric meridional coordinate y_a . On using the recurrence relations for the Hermite functions the system is reduced to the following set of equations for the unknowns $R_n(x)$

$$(\epsilon_a + \partial_x)R_0 + \frac{1}{2}Q_0(x) = 0 \quad (A.3a)$$

$$R_1(x) = 0 \quad (A.3b)$$

$$((2n - 1)\epsilon_a - \partial_x)R_n + \frac{1}{2}(n - 1)(Q_n + \sqrt{\frac{n}{n - 1}}Q_{n-2}) = 0, n = 2, 3, \dots \quad (A.3c)$$

The forcing Q of the atmospheric component is obtained from the spectral representation of the SST in the ocean and the $Q_n(x)$ in (A.3) are written as

$$Q_n(x) = \sum_{i=0} \sum_{j=0} C_i(2x - 1)c_{nj}q_{ij}, \quad (A.4)$$

the coefficients c_{nj} result from the projection of oceanic onto atmospheric Hermite functions. Solving (A.3) in terms of the coefficients q_{ij} the zonal windstress component becomes

$$\begin{aligned} u_a(x, y_a, t) &= \sum_{n=0} (R_n(x, t) - \sqrt{\frac{n+2}{n+1}}R_{n+2}(x, t))\psi_n(y_a) \\ &= \sum_{i=0} \sum_{j=0} \mathcal{A}_{ij}(x, y_a)q_{ij}(t), \end{aligned} \quad (A.5)$$

with \mathcal{A}_{ij} given by

$$\mathcal{A}_{ij}(x, y_a) = \sum_{n=0} (R_n^{ij}(x) - \sqrt{\frac{n+2}{n+1}} R_{n+2}^{ij}(x)) \psi_n(y_a). \quad (A.6)$$

The zonal windstress forcing τ^x , (7), has atmospheric meridional scales. Hence, to obtain the correct ocean forcing, τ^x has to be projected onto the oceanic Hermite functions i.e.

$$\tau^x(x, y_a, t) = \sum_{n=0} (\tau_n^{ext}(t) + \mu A_n(x, t)) \psi_n(y)$$

with

$$\tau_n^{ext}(t) = \int_{-\infty}^{\infty} \tau^{ext}(y_a, t) \psi_n(y) dy$$

and

$$A_n(x, t) = \int_{-\infty}^{\infty} u_a(x, y_a, t) \psi_n(y) dy.$$

Substitution of the expression for u_a yields

$$A_n(x, t) = \sum_{i=0} \sum_{j=0} a_{ij}^n(x) q_{ij}(t)$$

where $a_{ij}^n(x)$ is given by

$$a_{ij}^n(x) = \int_{-\infty}^{\infty} \mathcal{A}_{ij}(x, y_a) \psi_n(y) dy,$$

with \mathcal{A}_{ij} as in (A.5). The surface layer velocities in the ocean are solved directly in terms of the applied windstress forcing, i.e.

$$u_s = \frac{\gamma_s \Lambda_s}{\epsilon_s^2 \Lambda_s^2 + y^2} (\epsilon_s \Lambda_s \tau^x - y \tau^y) \quad (A.7a)$$

$$v_s = \frac{\gamma_s}{\epsilon_s^2 \Lambda_s^2 + y^2} (\epsilon_s \Lambda_s \tau^y - y \tau^x) \quad (A.7b)$$

To solve the equations (3), new variables r and s are introduced $u = r + s$ and $h = r - s$. The unknowns r are expanded into $\psi_j(y)$ and using the recurrence relations for the Hermite functions the system (3) is reduced to a set of equations for the unknowns $r_j(x)$, which becomes

$$(\delta \partial_t + \epsilon_o + \partial_x) r_0 - \frac{1}{2} \mathcal{F}_0(x) = 0 \quad (A.8a)$$

$$r_0(x=0) - \sum_{j=2} (j-1)^{-1} \mathcal{E}_j r_j(x=0) = 0 \quad (A.8b)$$

$$r_1(x) = 0 \quad (A.8c)$$

$$((2j-1)(\delta\partial_t + \epsilon_o) - \partial_x)r_j - \frac{1}{2}(j-1)(\mathcal{F}_j - \sqrt{\frac{j}{j-1}}\mathcal{F}_{j-2}) = 0 \quad (A.8d)$$

$$r_j(x=1) - \mathcal{E}_j r_0(x=1) = 0, \quad j = 2, 3, \dots \quad (A.8e)$$

The coefficients \mathcal{E}_j result from the discretization of the boundary conditions and are given by

$$\mathcal{E}_0 = 1, \quad \mathcal{E}_1 = 0, \quad \mathcal{E}_j = \sqrt{\frac{j}{j-1}}\mathcal{E}_{j-2}, \quad j = 2, 3, 4, \dots \quad (A.8f)$$

The unknowns r_j of the oceanic shallow water component are again expanded into Chebychev polynomials, i.e.

$$r_j(x) = \sum_{i=0} C_i(2x-1)r_{ij} \quad (A.9)$$

The SST-equation (6) is rewritten in terms of $\hat{T} = T - T_0$ and is, in addition to (A.8) solved by collocation. The solution vector \mathbf{z} , as presented in (11), contains the oceanic wave components r_{ij} and spectral coefficients of \hat{T} , q_{ij} as defined in (A.1). The collocation points in the meridional direction are the roots of the $(N_y + 1)$ th Hermite function, when the sum in (A.1) is truncated at $j = N_y$. The collocation points in the x -direction are the exterior gridpoints

$$x_k = -\cos\left(\frac{\pi k}{N_x}\right), \quad k = 0, \dots, N_x$$

The discretized set of equations thus contains $2N_x N_y$ unknowns, where N_x is the number of Chebychev polynomials and N_y the number of Hermite polynomials. The truncation of the number of basisfunctions in the spectral representation was determined from resolution studies of the first bifurcation point. While the results in section 3 were computed using $N_x = 17$ and $N_y = 41$, the sensitivity results presented in sections 4 and 5 were done for $N_x = 11$ and $N_y = 21$. Despite the infamous convergence properties of the Hermite functions the patterns and periods found for $N_x = 17$ and $N_y = 41$ differed only slightly from those at lower resolution.

Appendix B: The complete spectrum

The complete spectrum of the uncoupled ocean atmosphere model consists of eigenvalues originating from the SST-equation and from uncoupled ocean-dynamics. The latter were discussed by Moore (1968), Cane and Sarachik (1981), Cane and Moore (1981) and Neelin and Jin (1993) and are shown in Fig. 25a. The ocean-dynamics spectrum consists of ocean-basin modes, indicated by triangles in Fig. 25, and scattermodes. Characteristic feature of the scattermodes is their appearance as rays in the spectrum, centered around the stationary scattermode with the smallest damping rate. The number of rays is equal to the degrees of freedom in the meridional direction, while their length is determined by the zonal resolution of the model discretization (cf. Neelin and Jin (1993)). The uncoupled SST-spectrum is located near $Re(\sigma) = -2.8 \text{ year}^{-1}$ in panel (a). In Fig. 25b the fully developed spectrum at large coupling ($\mu = 0.74$) is plotted. The initially oscillatory instability has splitted into two stationary modes, which can be discerned to the right. The SST-related part of the spectrum shows the development of oscillatory modes which either grow or decay. This is more clearly seen in Fig. 25d, where, in the fast-wave limit, the ocean-dynamics modes have been filtered from the spectrum. The leading modes are high-frequency asymmetric modes, related to the meridional advection terms in the SST-equation. In the fast-SST limit, Fig. 25c, the SST-modes have been filtered, showing that, apart from the selection of the ENSO-mode, the spectrum is hardly affected by coupling. The ocean-basin modes, relevant in several previous studies (Cane *et al.*, 1990; Dijkstra and Neelin, 1998), are indicated by triangles.

References

- Battisti, D. (1988). The dynamics and thermodynamics of a warming event in a coupled tropical ocean/atmosphere model. *J. Atm. Sc.*, **45**, 2889–2919.
- Battisti, D. and Hirst, A. (1989). Interannual variability in a tropical atmosphere-ocean model: Influence of the basic state, ocean geometry and nonlinearity. *J. Atm. Sc.*, **46**, 1687–1712.
- Blanke, B., Neelin, J. D., and Gutzler, D. (1997). Estimating the effect of stochastic wind stress forcing on ENSO irregularity. *J. Clim.*, **10**, 1473–1486.
- Cane, M. (1992). Comments on "The fast-wave limit and interannual oscillation". *J. Atm. Sc.*, **49**, 1947–1949.
- Cane, M. and Moore, D. (1981). A note on low-frequency equatorial basin modes. *J. Phys. Ocean.*, **11**, 1578–1584.
- Cane, M. and Sarachik, E. (1981). The response of a linear baroclinic equatorial ocean to periodic forcing. *J. Mar. Res.*, **39**, 651–693.
- Cane, M. and Zebiak, S. (1985). A theory for El Niño and the Southern Oscillation. *Science*, **228**, 1084–1087.
- Cane, M., Münnich, M., and Zebiak, S. (1990). Study of self-excited oscillations of the tropical ocean-atmosphere system. Part I: Linear analysis. *J. Atm. Sc.*, **47**, 1562–1577.
- Dijkstra, H. and Neelin, J. D. (1995a). Coupled ocean-atmosphere models and the tropical climatology, part II: Why the cold tongue is in the east. *J. Clim.*, **8**, 1343–1359.
- Dijkstra, H. and Neelin, J. D. (1995b). On the attractors of an intermediate coupled ocean-atmosphere model. *Dyn. Oc. Atm.*, **22**, 19–48.
- Dijkstra, H. and Neelin, J. D. (1998). Coupled processes and the tropical climatology. Part III: Instabilities of the fully coupled climatologies. *J. Clim.*, *submitted*.
- Gill, A. (1980). Some simple solutions for heat induced tropical circulation. *Quart. J. Roy. Meteor. Soc.*, **106**, 447–462.
- Hao, Z., Neelin, J. D., and Jin, F.-F. (1993). Nonlinear tropical air-sea interaction in the fast-wave limit. *J. Clim.*, **6**, 1523–1544.
- Hirst, A. (1988). Slow instabilities in tropical ocean basin-global atmosphere models. *J. Atm. Sc.*, **45**, 830–852.
- Hirst, A. C. (1986). Unstable and damped equatorial modes in simple coupled ocean-atmosphere models. *J. Atm. Sc.*, **43**, 606–630.

- Jin, F.-F. (1996). Tropical ocean-atmosphere interaction, the Pacific Cold Tongue, and the El Niño/Southern Oscillation. *Science*, **274**, 76–78.
- Jin, F.-F. (1997a). An equatorial recharge paradigm for ENSO: Part I: Conceptual Model. *J. Atm. Sc.*, **54**, 811–829.
- Jin, F.-F. (1997b). An equatorial recharge paradigm for ENSO: Part II: A stripped-down coupled model. *J. Atm. Sc.*, **54**, 830–8847.
- Jin, F.-F. and Neelin, J. D. (1993a). Modes of interannual tropical ocean-atmosphere interaction - a unified view. Part I: Numerical results. *J. Atm. Sc.*, **50**, 3477–3503.
- Jin, F.-F. and Neelin, J. D. (1993b). Modes of interannual tropical ocean-atmosphere interaction—a unified view. Part III: Analytical results in fully coupled cases. *J. Atm. Sc.*, **50**, 3523–3540.
- Jin, F.-F., Neelin, J. D., and Ghil, M. (1994). El Niño on the devil’s staircase: Annual subharmonic steps to chaos. *Science*, **264**, 70–72.
- Kirtman, B. (1997). Oceanic Rossby wave dynamics and the ENSO period in a coupled model. *J. Clim.*, **10**, 1690–1704.
- Latif, M., Sterl, A., Maier-Reimer, E., and Junge, M. (1993). Structure and predictability of the El Niño/Southern Oscillation phenomenon in a coupled ocean-atmosphere general circulation model. *J. Clim.*, **6**, 700–708.
- Moore, D. (1968). *Planetary-gravity waves in an equatorial ocean. PhD Thesis.* Harvard University, Cambridge, MA.
- Münnich, M., Cane, M., and Zebiak, S. (1991). A study of self-excited oscillations of the tropical ocean-atmosphere system. Part II: Nonlinear cases. *J. Atm. Sc.*, **48**, 1238–1248.
- Neelin, J., Battisti, D., Hirst, A., Jin, F., Wakata, Y., Yamagata, T., and Zebiak, S. (1997). ENSO Theory. *J. Geoph. Res.*, *submitted*.
- Neelin, J. D. (1991). The slow sea surface temperature mode and the fast-wave limit: Analytic theory for tropical interannual oscillations and experiments in a hybrid coupled model. *J. Atm. Sc.*, **48**, 584–606.
- Neelin, J. D. and Dijkstra, H. (1995). Coupled ocean-atmosphere models and the tropical climatology, part I: The dangers of flux-correction. *J. Clim.*, **8**, 1325–1342.
- Neelin, J. D. and Jin, F. (1993). Modes of interannual tropical ocean-atmosphere interaction—a unified view. Part II: Analytical results in the weak-coupling limit. *J. Atm. Sc.*, **50**, 3504–3522.

- Neelin, J. D., Latif, M., and Jin, F. (1994). Dynamics of coupled ocean-atmosphere models: The tropical problem. *Ann. Rev. Fluid Mech.*, **26**, 617–659.
- Philander, S., Pacanowski, R., Lau, N., and Nath, M. (1992). Simulation of ENSO with a global atmospheric GCM coupled to a high-resolution tropical Pacific ocean GCM. *J. Clim.*, **5**, 308–329.
- Schopf, P. and Suarez, M. (1988). Vacillations in a coupled ocean-atmosphere model. *J. Atm. Sc.*, **45**, 549–566.
- Schopf, P. and Suarez, M. (1990). Ocean wave dynamics and the time scale of ENSO. *J. Phys. Ocean.*, **20**, 629–645.
- Suarez, M. and Schopf, P. S. (1988). A delayed action oscillator for ENSO. *J. Atm. Sc.*, **45**, 3283–3287.
- Terray, L., Thual, O., Belamari, S., Déqué, M., Dandin, P., Delecluse, P., and Levy, C. (1995). Climatology and interannual variability simulated by the ARPEGE-OPA coupled model. *Clim. dyn.*, **12**, 487–505.
- Tziperman, E., Stone, L., Cane, M., and Jarosh, H. (1994). El Niño chaos: overlapping of resonances between the seasonal cycle and the Pacific ocean-atmosphere oscillator. *Science*, **264**, 72–74.
- Wyrtki, K. (1975). El Niño - The dynamic response of the equatorial Pacific ocean to atmospheric forcing. *J. Phys. Ocean.*, **5**, 572–584.
- Wyrtki, K. (1985). Water displacements in the Pacific and the genesis of El Niño cycles. *J. Geoph. Res.*, **91**, 7129–7132.
- Zebiak, S. and Cane, M. (1987). A model El Niño-Southern Oscillation. *Monthly Weather Review*, **115**, 2262–2278.

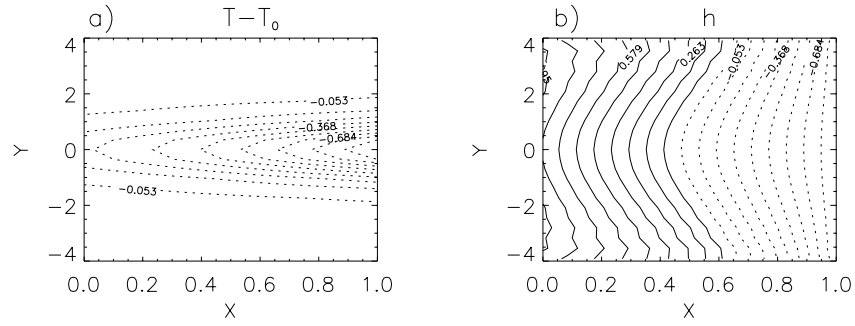


Figure 1: *The climatology due to the external wind forcing only. (a) The temperature deviation $T - T_0$. The maximum amplitude is $4.5\text{ }^\circ\text{C}$ and contour levels (contour interval 0.11) are with respect to this maximum. (b) Thermocline depth. The maximum amplitude is 22.5 m and contour levels (contour interval 0.11) are with respect to this maximum.*

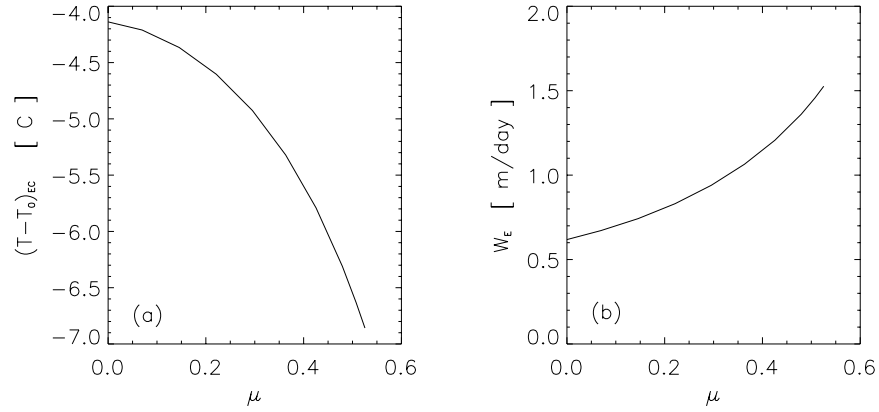


Figure 2: Eastern Pacific ($x = 0.8$) equatorial SST deviation from T_0 (a) and upwelling (b) as a function of the coupling strength μ .

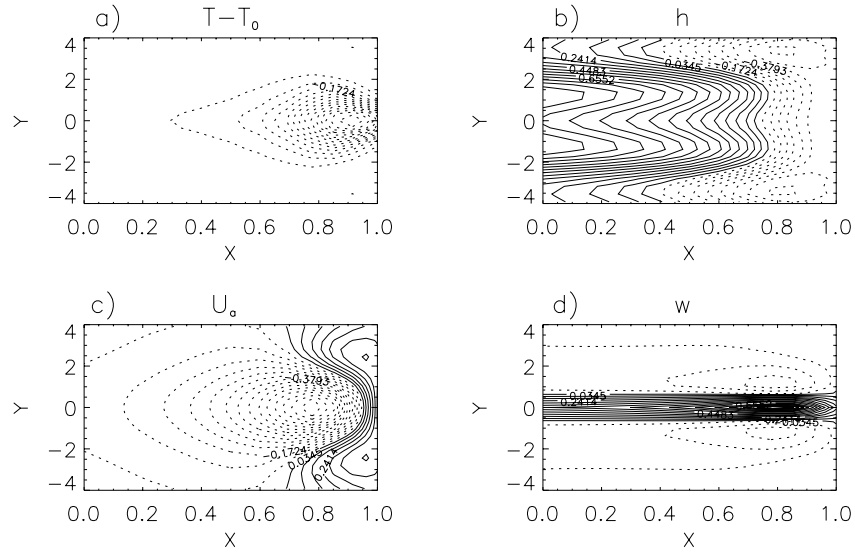


Figure 3: The climatology at standard parameter values and $\mu = 0.5$. (a) $T - T_0$; maximum 6.6°C (contour interval 0.069). (b) Thermocline depth; maximum 82.3 m . (c) Zonal windstress u_a ; maximum 9.5 m/s . (d) Vertical velocity; maximum 1.44 m/day

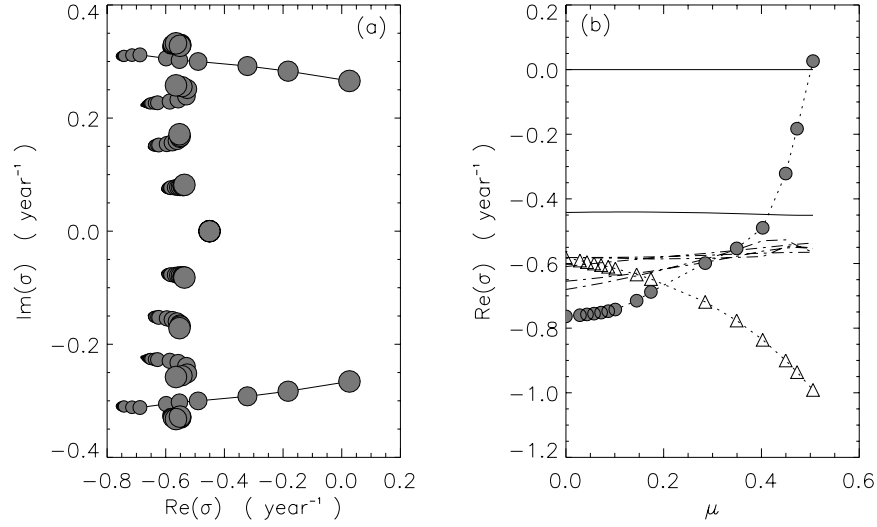


Figure 4: (a) Plot of the eigenvalues for the six leading eigenmodes in the $(\text{Re}(\sigma), \text{Im}(\sigma))$ -plane. Values of the coupling strength μ are represented by dot size (smallest dot is the uncoupled case for each mode ($\mu = 0$), largest is the fully coupled case at the Hopf bifurcation ($\mu_H = 0.503$)). The Hopf-bifurcation that yields the ENSO mode occurs where the path of one eigenvalue first crosses $\text{Re}(\sigma) = 0$. (b) The growth rate of the leading modes as a function of coupling strength.

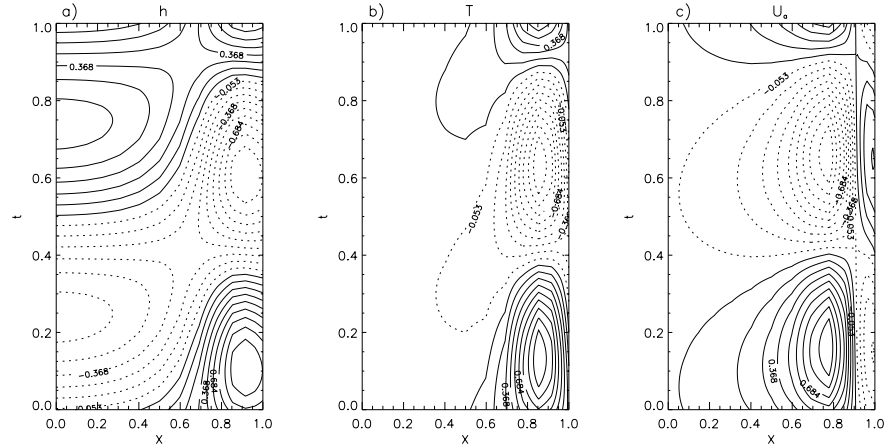


Figure 5: Time-longitude diagram at the equator of the anomalies of (a) SST (max = 1.4°C), (b) thermocline depth (max. = 9.5 m), and (c) zonal windstress (max. = 3.0 m/s). The period of the oscillation is 3.7 years.

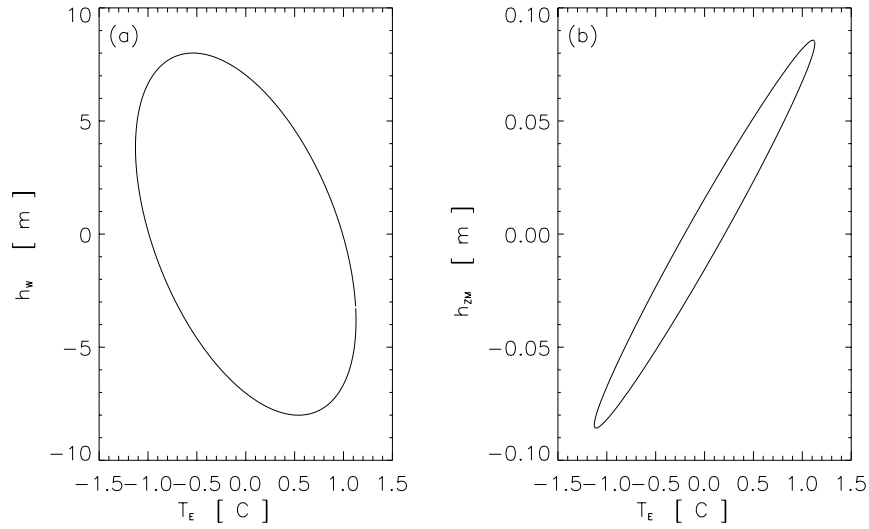


Figure 6: (a) Phase relation between the equatorial thermocline depth anomaly in the western part of the basin and the SST anomaly in the east. (b) The phase relation between the zonally averaged equatorial thermocline anomaly h_{ZM} and SST anomaly in the east (T_E). Note that the amplitudes in both panels are arbitrary, but that their ratio is fixed. The direction of rotation is clockwise in both cases.

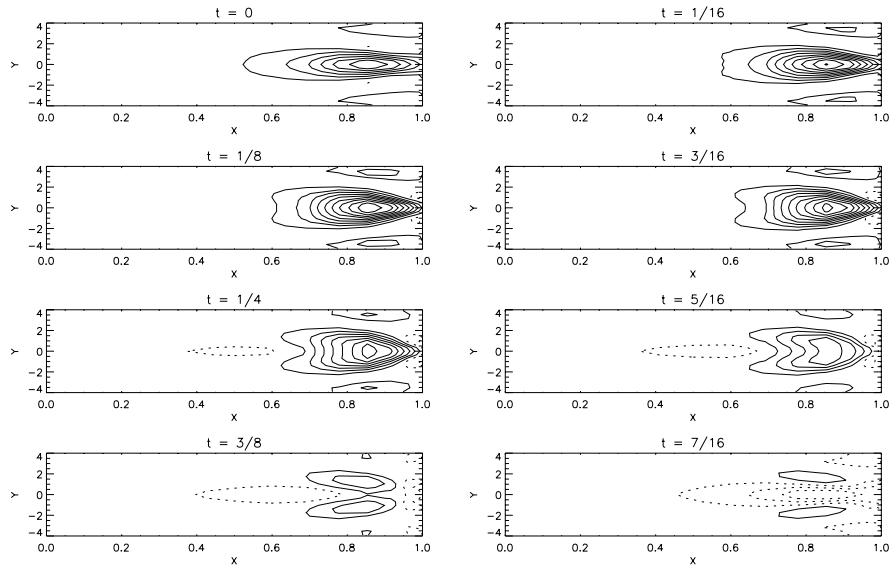


Figure 7: Planforms of the SST anomaly during the oscillation. Drawn (dotted) lines represent warm (cold) anomalies.

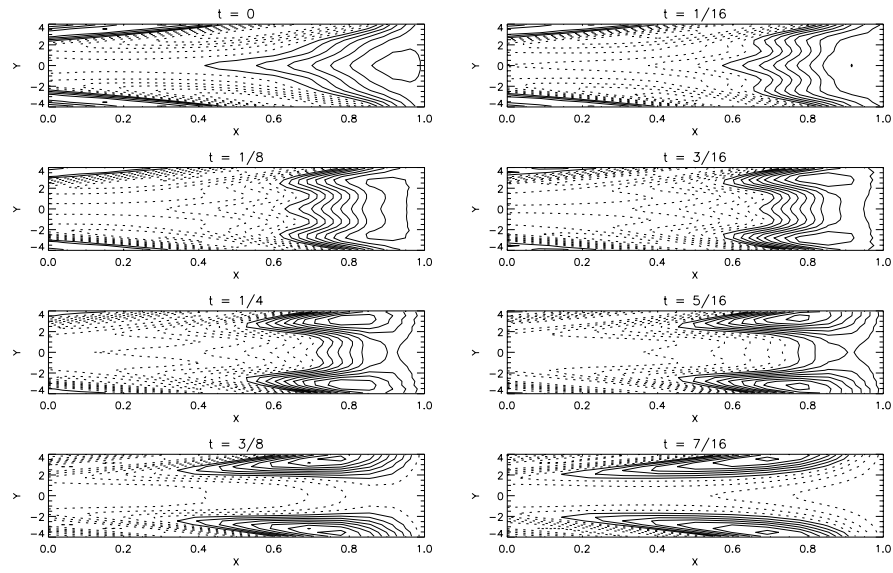


Figure 8: Planforms of the thermocline depth anomaly during the oscillation. Drawn (dotted) lines represent positive (negative) anomalies.

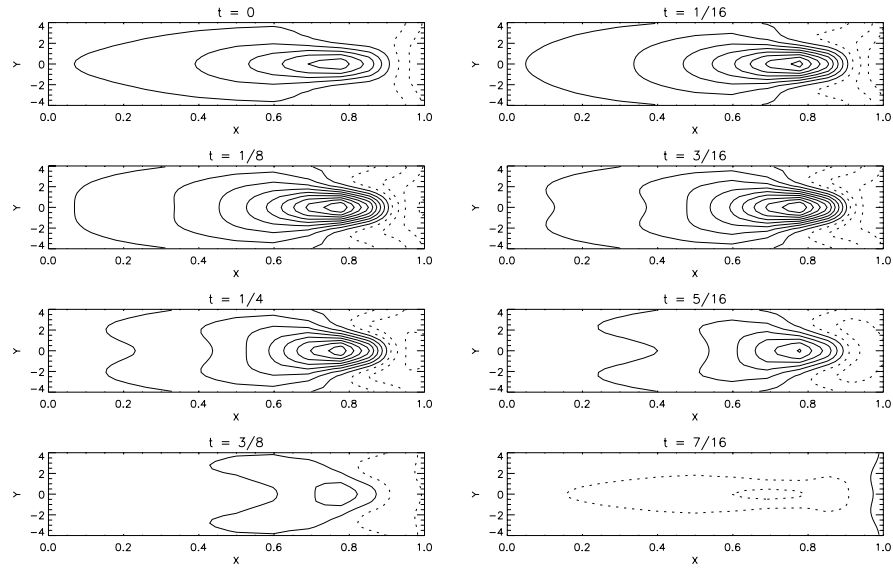


Figure 9: Planforms of the windstress anomaly during the oscillation. Drawn (dotted) lines represent anomalous westerlies (easterlies).

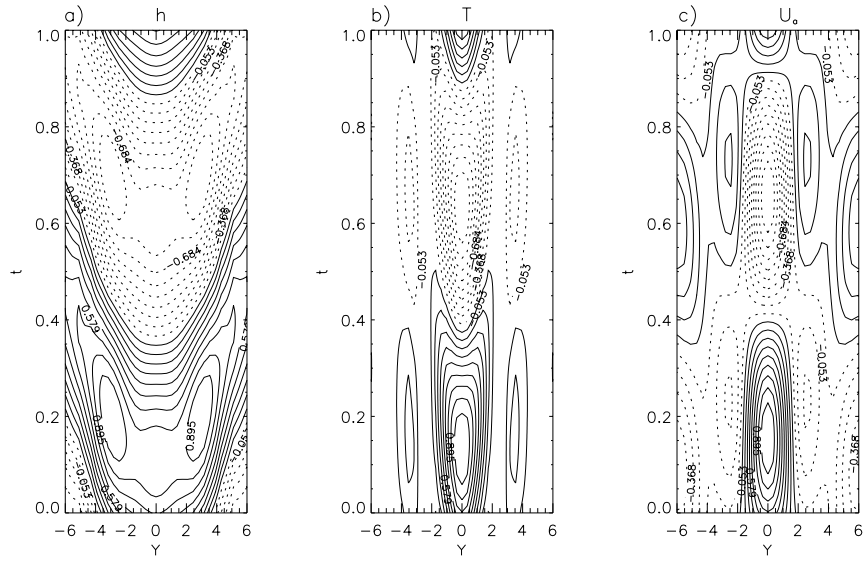


Figure 10: *Time-latitude diagram in the eastern part of the basin ($x = 0.85$) of the anomalies of (a) thermocline depth, (b) SST and (c) zonal windstress.*

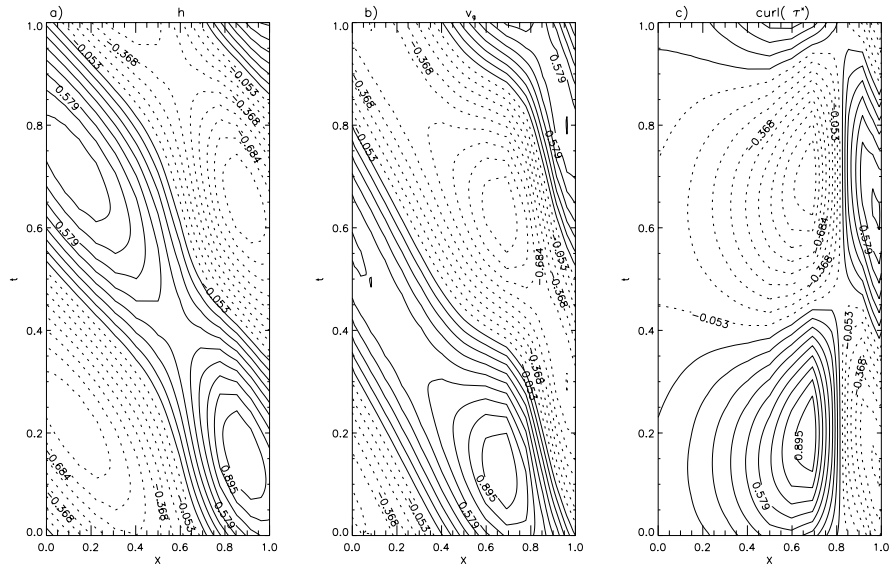


Figure 11: *Time-longitude diagrams at 8N of the anomalies of (a) thermocline depth, (b) the geostrophic meridional transport and the (c) curl of the anomalous windstress.*

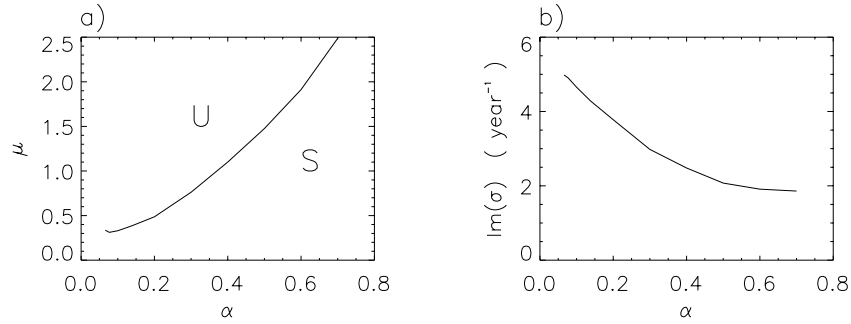


Figure 12: Variation of α : (a) The path of the Hopf-bifurcation in the $(\alpha - \mu)$ -plane. S (U) indicates regions of linear (un)stable climatologies. (b) The period of the oscillation at the Hopf-bifurcation as function of α .

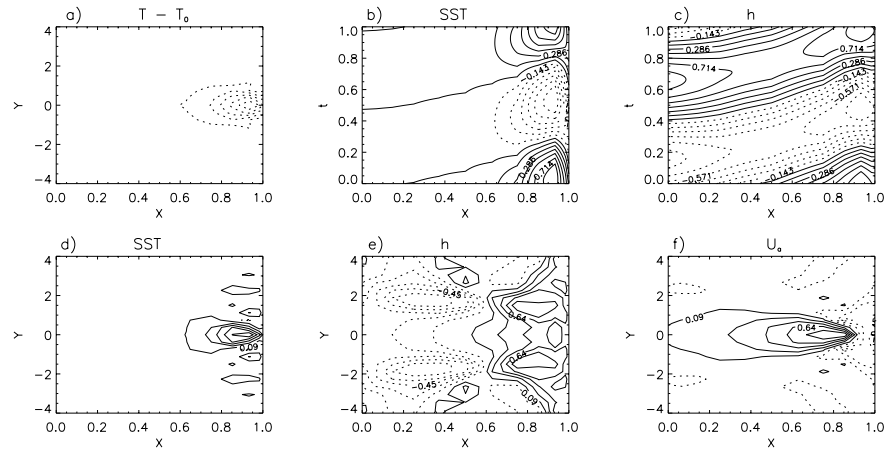


Figure 13: (a) The climatological departure of SST from radiative equilibrium at the Hopf-bifurcation point for $\alpha = 0.7$ (maximum = 3.8 °C). The equatorial time-longitude diagram of SST anomaly (b) and thermocline depth anomaly (c) for the climatology in (a). Patterns of anomalies of SST (d), h (e) and u_a (f) at time $t = 0$ for $\alpha = 0.7$.

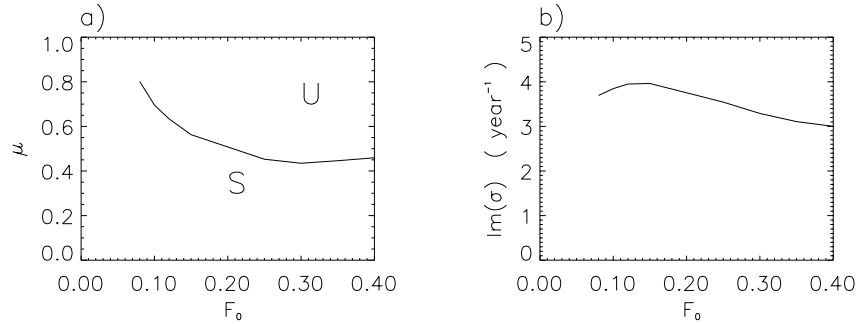


Figure 14: Variation of F_0 : (a) The path of the Hopf-bifurcation in the (F_0, μ) -plane. S (U) indicates regions of linear (un)stable climatologies. (b) The period at the Hopf-bifurcation as function of F_0 .

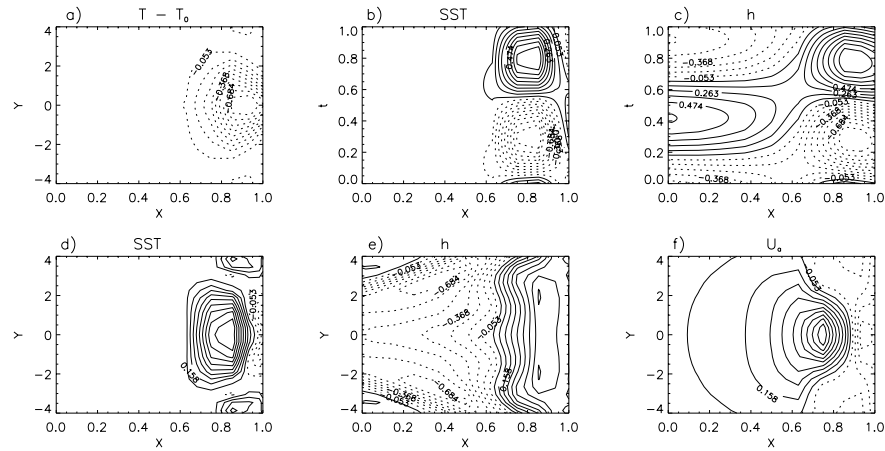


Figure 15: (a) The climatological departure of SST from radiative equilibrium at the Hopf-bifurcation point for $F_0 = 0.4$ (maximum = $11.0\text{ }^\circ\text{C}$). The equatorial time-longitude diagram of SST anomaly (b) and thermocline depth anomaly (c) for the climatology in (a). Patterns of anomalies of SST (d), h (e) and u_a (f) at time $t = 0$ for $F_0 = 0.4$.

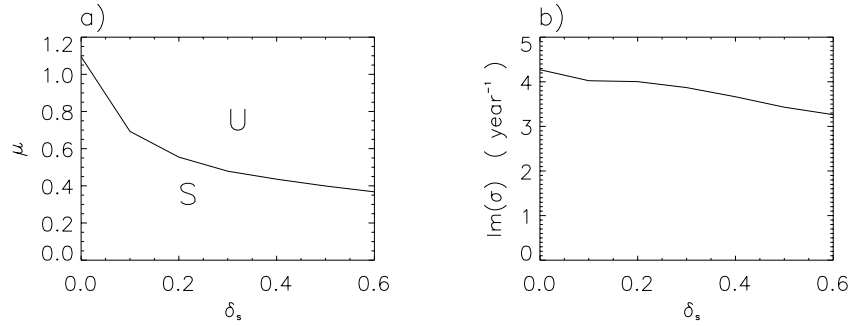


Figure 16: Variation of δ_s : (a) The path of the Hopf-bifurcation in the (δ_s, μ) -plane. *S* (*U*) indicates regions of linear (un)stable climatologies. (b) The period at the Hopf-bifurcation as function of δ_s .

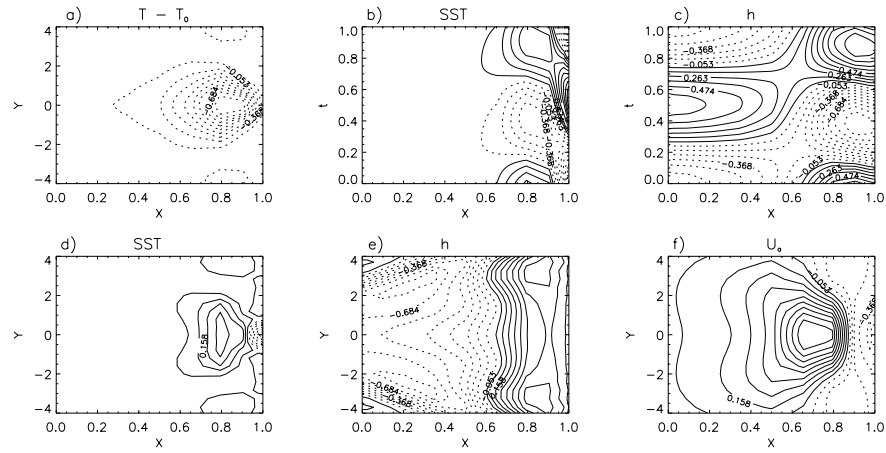


Figure 17: (a) The climatological departure of SST from radiative equilibrium at the Hopf-bifurcation point for $\delta_s = 0.6$ (maximum = 5.6 °C). The equatorial time-longitude diagram of SST anomaly (b) and thermocline depth anomaly (c) for the climatology in (a). Patterns of anomalies of SST (d), h (e) and u_a (f) at time $t = 0$ for $\delta_s = 0.6$.

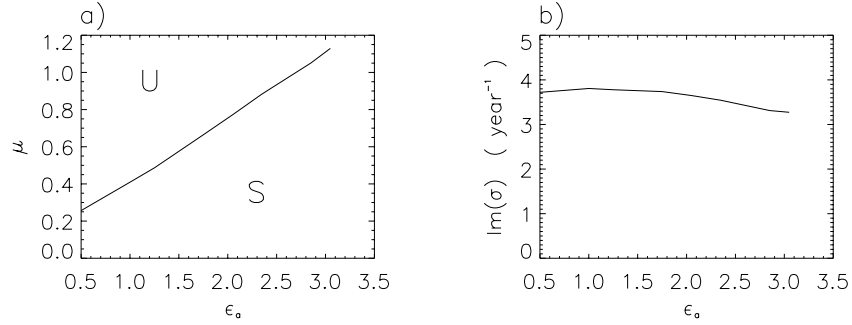


Figure 18: Variation of ϵ_a : (a) The path of the Hopf-bifurcation in the (ϵ_a, μ) -plane. S (U) indicates regions of linear (un)stable climatologies. (b) The period at the Hopf-bifurcation as function of ϵ_a .

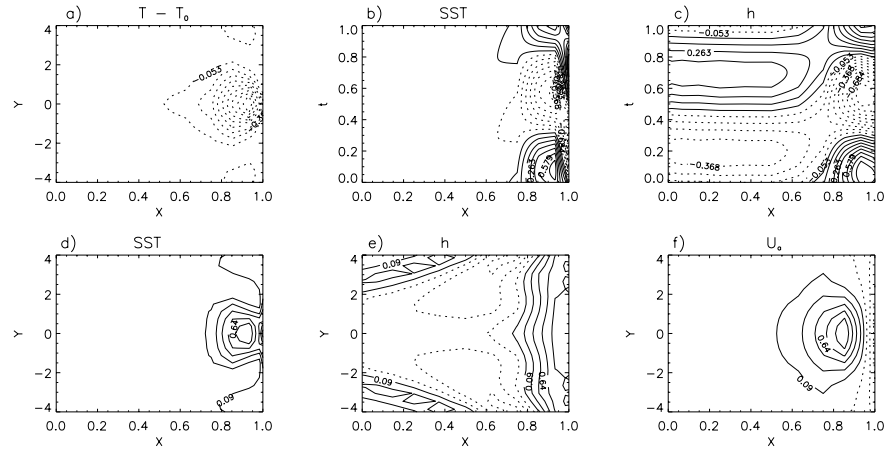


Figure 19: (a) The climatological departure of SST from radiative equilibrium at the Hopf-bifurcation for $\epsilon_a = 3.05$ (maximum = 6.7°C). The equatorial time-longitude diagram of SST anomaly (b) and thermocline depth anomaly (c) for the climatology in (a). Patterns of anomalies of SST (d), h (e) and u_a (f) at time $t = 0$ for $\epsilon_a = 3.05$.

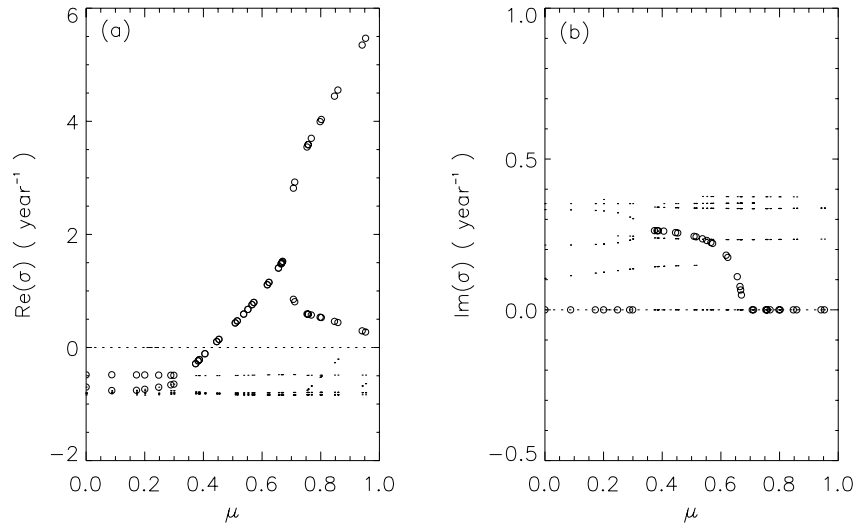


Figure 20: *The growthrates and frequencies of the leading eigenvalues as a function of coupling strength μ for the fully coupled case.*

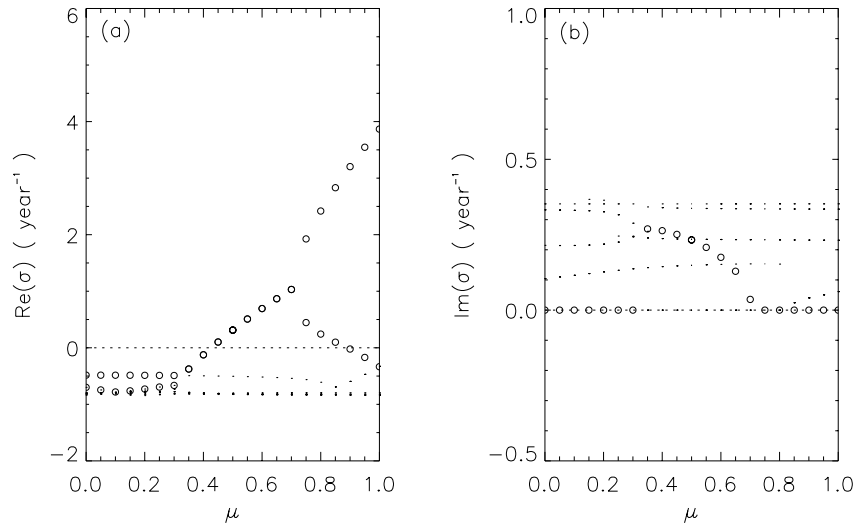


Figure 21: *The growthrates and frequencies of the leading eigenvalues as a function of coupling strength μ for the flux-corrected case. The growth rates and frequencies of the leading mode are indicated by open circles. The other modes are indicated by dots. Near $\mu = 0.35$ the ENSO mode emerges from the spectrum, being heavily damped at $\mu = 0$.*

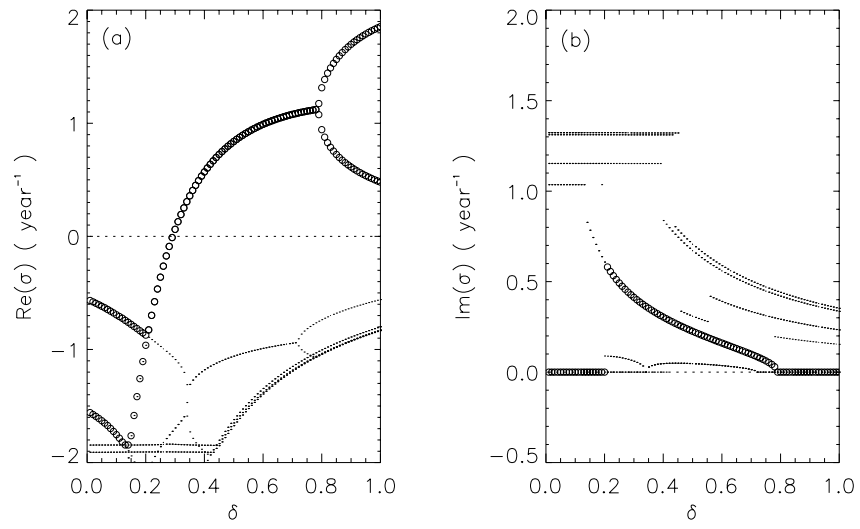


Figure 22: *The growthrates and frequencies of the leading eigenvalues as a function of δ for the flux-corrected case.*

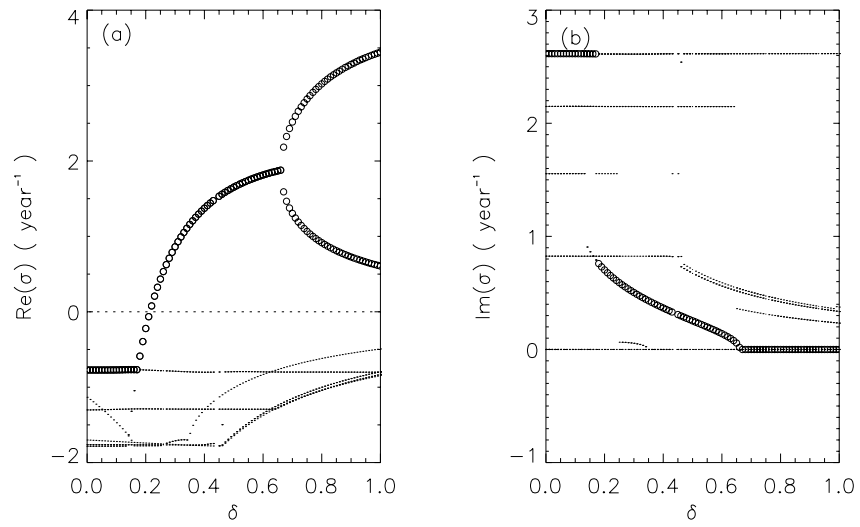


Figure 23: *The growthrates and frequencies of the leading eigenvalues as a function of δ for the fully-coupled case.*

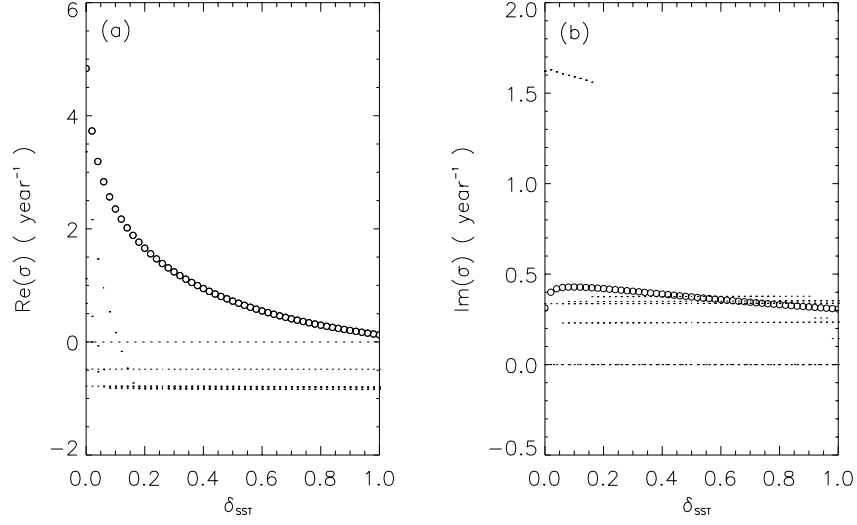


Figure 24: The growth rates and frequencies of the leading eigenvalues as a function of δ_{sst} for the fully-coupled case.

$\epsilon_o = r^* L / c_0 = 0.1$	$\delta = 1.0$	$F_0 = 0.2$
$\epsilon_a = A^* L / c_a = 1.25$	$\alpha = L_y / L_a = 0.2$	$\mu = \alpha_T \gamma_\tau \Delta T L^2 / (c_a^2 c_0^2) = 0.503$
$\epsilon_s = \epsilon_s^* L / c_0 = 37.5$	$\Lambda_s = L_y / L = 2.0 \cdot 10^{-2}$	$\gamma_s = H_2 / H_1 = 3.0$
$\delta_s = 0.3$	$\alpha_w = H_1 / \tilde{H} = 1.0$	$\delta_w = 5.0 \cdot 10^{-2}$
$\eta_1 = H / H^* = 5.01$	$\eta_2 = h_0 / H^* = 0.5$	$T_{s0} = 23.0$
$\epsilon_T = \epsilon_w L / c_0 = 0.694$	$T_0 = 30.0$	

Table 1: Values of dimensionless parameters

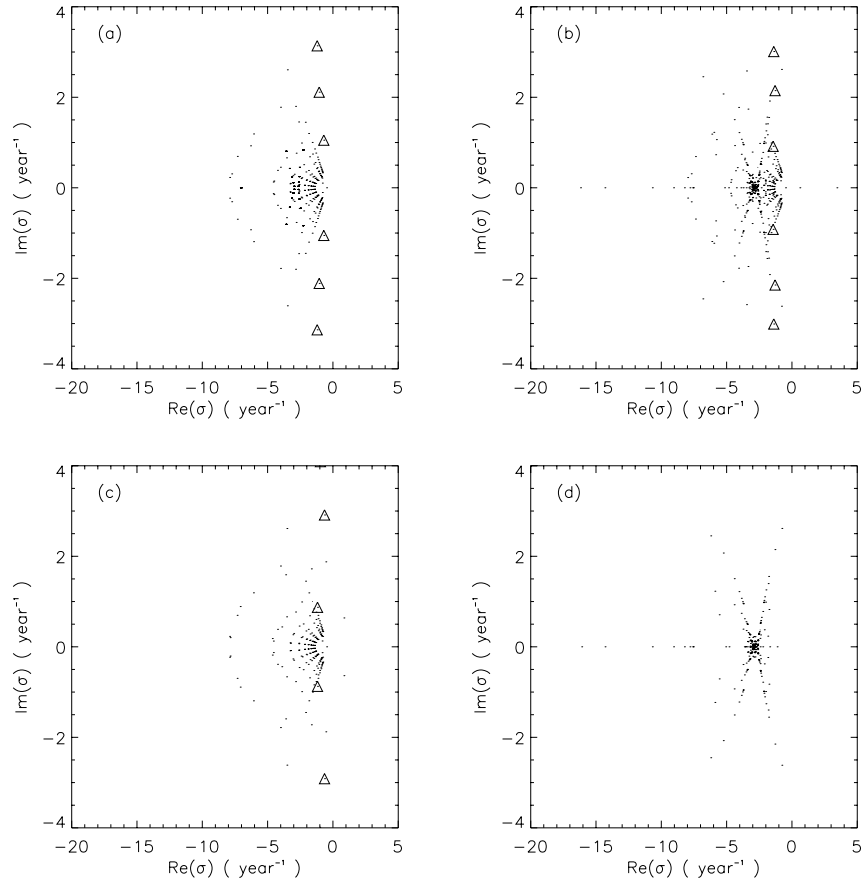


Figure 25: *The complete spectrum of the model for 4 distinctive cases. (a). Uncoupled ($\mu = 0$). (b). Fully coupled, $\mu = 0.74, \delta = 1.0, \delta_{sst} = 1.0$. (c). Fast SST limit, $\delta_{sst} = 0.0$. (d) Fast wave limit, $\delta = 0.0$*